JACS
JOURNAL OF THE AMERICAN CHEMICAL SOCIETY
Article
pubs.acs.org/JACS

Half-Unit-Cell α-Fe_2O_3 Semiconductor Nanosheets with Intrinsic and Robust Ferromagnetism

Weiren Cheng,[†] Jingfu He,[†] Tao Yao, Zhihu Sun, Yong Jiang, Qinghua Liu,* Shan Jiang, Fengchun Hu, Zhi Xie, Bo He, Wensheng Yan,* and Shiqiang Wei*

National Synchrotron Radiation Laboratory, University of Science and Technology of China, Hefei 230029, Anhui, People's Republic of China

Supporting Information

ABSTRACT: The synthesis of atomically thin transition-metal oxide nanosheets as a conceptually new class of materials is significant for the development of next-generation electronic and magnetic nanodevices but remains a fundamental chemical and physical challenge. Here, based on a "template-assisted oriented growth" strategy, we successfully synthesized half-unit-cell nanosheets of a typical transition-metal oxide α-Fe_2O_3 that show robust intrinsic ferromagnetism of 0.6 μ_B/atom at 100 K and remain ferromagnetic at room temperature. A unique surface structure distortion, as revealed by X-ray absorption spectroscopy, produces nonidentical Fe ion environments and induces distance fluctuation of Fe ion chains. First-principles calculations reveal that the efficient breaking of the quantum degeneracy of Fe 3d energy states activates ferromagnetic exchange interaction in these $Fe_{5\text{-}co}$−O−$Fe_{6\text{-}co}$ ion chains. These results provide a solid design principle for tailoring the spin-exchange interactions and offer promise for future semiconductor spintronics.

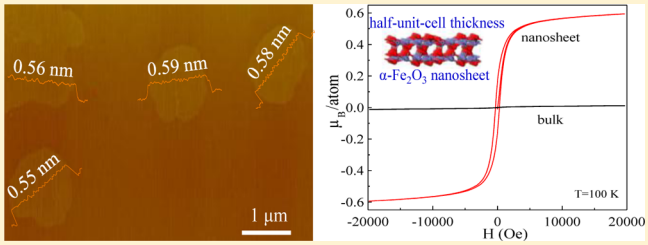

INTRODUCTION

The successful preparation of two-dimensional (2D) materials such as graphene, metal chalcogenides, and carbon nitrides has opened a new pathway for creating high-performance nanodevices.[1−3] The 2D nanosheets exhibit fascinating physical and chemical properties including the direct band gap transition, superior electron mobility, and high catalytic activity, due to the quantum confinement and maximum surface area.[4−7] Benefiting from their lamellar structure, these nanosheets with thickness smaller than one-unit-cell height can be easily obtained via the top-down methods of mechanic and/or liquid exfoliation from their bulk materials.[8−11] Besides these well-known 2D materials, it is highly desired to obtain novel 2D nanosheets from the numerous nonlayered materials, especially the earth-abundant transition-metal oxides (TMOs) that are widely investigated and host rich chemistry and physics. It has been reported that their electronic and magnetic properties are extremely sensitive to the dimensionality of the materials,[12,13] which provides new routes to manipulate these ground states by confining their thickness to a few atomic layers. However, the traditional exfoliation is fairly difficult to achieve atomically thin TMO nanosheets, owing to the hard and inefficient cleavage of the strong inherent chemical bonding.

Recently, great efforts have been made to fabricate the first-row 3d TMO ultrathin nanosheets, mainly based on the liquid exfoliation followed by topochemical transformation. For example, Co_3O_4 nanosheets with a thickness of 1.5 nm have been synthesized after the initial liquid exfoliation of $Co(OH)_2$, and this Co_3O_4 nanosheet was shown to facilitate Li^+ ion diffusion and electron transport in lithium energy storage applications.[14] By means of a structural phase transition-assisted liquid exfoliation strategy, monoclinic VO_2 nanosheets with a thickness of ca. 3.0 nm have been synthesized, which exhibit half-metallic character and a thermally induced phase transition.[15] So far, the reported 3d TMO nanosheets have thicknesses as large as several nanometers with several-to-dozens of atomic layers because of the strong interlayer bonding compared with the van der Waals' force. In contrast to these top-down methods, the bottom-up synthetic strategy of epitaxial growth has been demonstrated to be an effective way for growing thinner layered material.[16,17] Therefore, if the atomically thin layer of 3d transition-metal hydroxide (MOOH), which has very weak hydrogen bonding between adjacent layers,[18,19] can be orientedly grown at first, its corresponding TMO ultrathin nanosheets could be easily achieved by a subsequent process of topochemical transformation.

Motivated by the above consideration, on the basis of a "template-assisted oriented growth" strategy, we report for the first time the synthesis of atomically thin 3d TMO nanosheets with only half-unit-cell thickness, taking α-Fe_2O_3 as an example. Remarkably, the synthesized half-unit-cell α-Fe_2O_3 semiconductor nanosheets with only two Fe ion layers exhibit the robust intrinsic ferromagnetism of 0.6 μ_B saturation magnetic moment at 100 K, along with the remaining ferromagnetic

Received: April 24, 2014
Published: July 8, 2014

   dx.doi.org/10.1021/ja504088n | J. Am. Chem. Soc. 2014, 136, 10393−10398

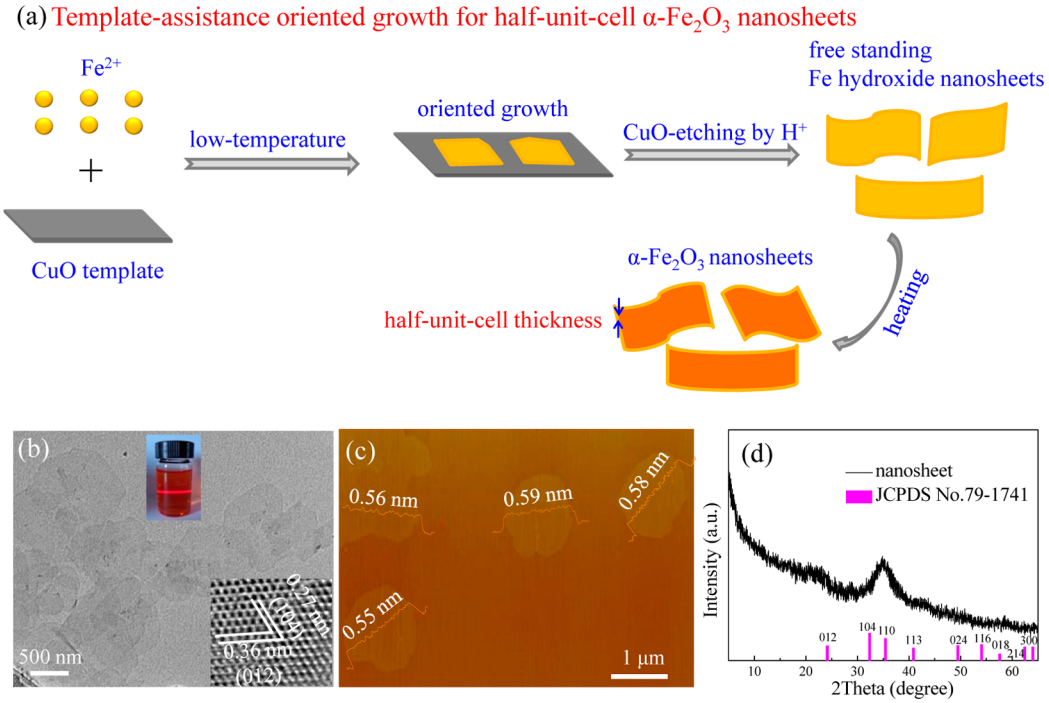

Figure 1. Synthesis, morphology, and structure of the half-unit-cell α-Fe_2O_3 nanosheets. (a) Schematic of synthesis strategy of α-Fe_2O_3 nanosheets. (b) TEM image of the α-Fe_2O_3 nanosheets. The insets show the HRTEM image and the Tyndall effect of the α-Fe_2O_3 nanosheets. (c) AFM image and (d) XRD pattern of the α-Fe_2O_3 nanosheets.

response at room temperature. In these synthesized α-Fe_2O_3 nanosheets, a large surface structural distortion is revealed to break the degenerate states of Fe ions into two groups: five-fold- and six-fold-coordinated. As a result, an efficient electron exchange between the five- and neighboring six-coordinated Fe ions is realized to activate the ferromagnetic interaction along the $Fe_{5\text{-}co}$−O−$Fe_{6\text{-}co}$ chains with a saturated moment of 0.6 μ_B, much higher than the available values reported so far. Our results not only open up new possibilities for manipulation of ferromagnetism in nanomaterials but also provide a new candidate for next-generation nano-spintronic devices.

RESULTS AND DISCUSSION

As depicted in Figure 1a, the ultrathin half-unit-cell α-Fe_2O_3 nanosheets were synthesized by controlling the gentle CuO-template-assisted growth in combination with a subsequent hydrothermal process. The morphology and structural information about the CuO template are included in S2 of the Supporting Information. The initial nanosheet seeds nucleate at the CuO template surface due to the interfacial reactions of Fe^{2+} hydrolysis. Then, the subsequently adsorbed ferrous ions enabled oriented growth at the interface of an assisted template by the mutually promoted slow interfacial reactions of Fe^{2+} hydrolysis and CuO etching process at a low temperature (25 °C) for a whole day, which was beneficial for synthesis of ultrathin nanosheets. After the CuO template etching out, a heating treatment was carried out for dehydrogenation of Fe hydroxide nanosheets to form the stable and freestanding α-Fe_2O_3 nanosheets (inset of Figure 1b). Detailed structure information on the synthesized α-Fe_2O_3 nanosheets is unraveled by the transmission electron microscopy (TEM), atomic force microscopy (AFM), and X-ray diffraction (XRD) measurements as shown in Figure 1b−d. Two lattice fringes of 0.27 and 0.36 nm correspond to the (104) and (012) planes of α-Fe_2O_3, respectively. According to the fast Fourier transform image (see S2 and Figure S5a of Supporting Information), it can be concluded that (110) facets were exposed. The lateral size of the α-Fe_2O_3 ultrathin nanosheets is up to about 1 μm (Figures 1b,c and S3). The statistical height profiles of nanosheets show a smooth 2D sheet with thickness in the range of 0.55−0.59 nm (Figures 1c and S4), which is very close to a half-unit-cell (two Fe ion layers) thickness of the α-Fe_2O_3 lattice. The XRD pattern of the α-Fe_2O_3 nanosheets by directly drying the nanosheet−water suspension exhibits only a broad and weak diffraction peak corresponding to the (110) orientation plane of α-Fe_2O_3 (Figure 1d), and the half-width of the diffraction peak is about 8.5°, corresponding to about a thickness of ca. 0.9 nm that is basically consistent with the AFM results. To further clarify the crystalline structure and orientation of α-Fe_2O_3 nanosheets, a layer-by-layer assembly strategy was employed for the sample preparation of XRD detection (see Figure S5b of Supporting Information).[15,20,21] The resulting XRD pattern clearly displays a highly (110) orientation and undoubtedly confirms that the hexagonal lattice structure of α-Fe_2O_3 is kept in the α-Fe_2O_3 nanosheets. Therefore, the above results demonstrate that ultrathin α-Fe_2O_3 nanosheets with half-unit-cell thickness are successfully synthesized. In comparison with the previous reports of α-Fe_2O_3 nanosheets with thickness ranging from several to tens of nanometers,[22−26] the success of our template-assisted oriented growth lies in the interacting promotion of CuO self-dissolution and Fe ion hydrolysis that makes the nanosheets intensively adjacent on the template surface to orient the growth and the low growth temperature that can effectively inhibit the growth of nanosheets along the third dimension.

To further examine the magnetic correlation in the α-Fe_2O_3 nanosheets, the temperature-dependent magnetization curves (M−T) and hysteresis loops (M−H) of the nanosheets and the

dx.doi.org/10.1021/ja504088n | J. Am. Chem. Soc. 2014, 136, 10393−10398

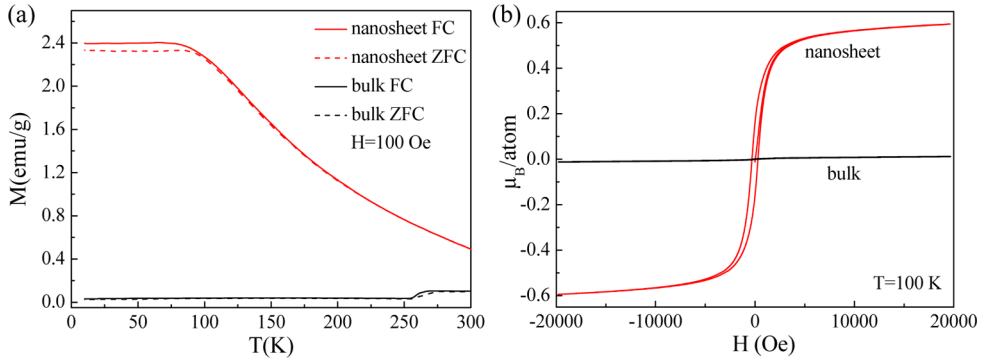

Figure 2. Magnetization measurements for the samples. (a) ZFC−FC magnetization curves and (b) hysteresis loops of nanosheet and bulk α-Fe_2O_3.

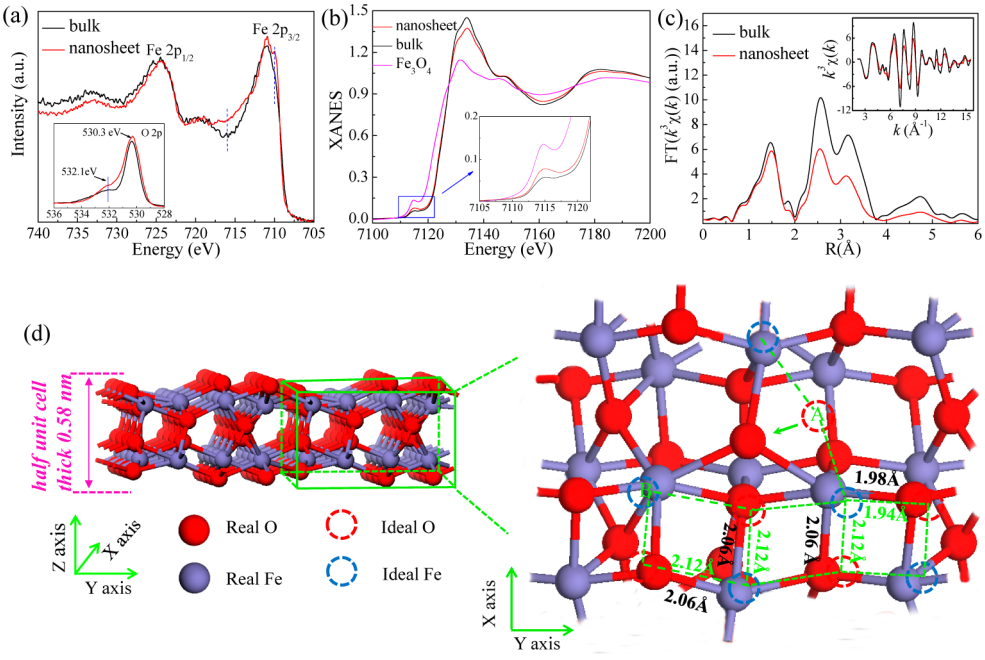

Figure 3. (a) XPS and (b) Fe *K*-edge XANES spectra of nanosheet and bulk α-Fe_2O_3 and Fe_3O_4 for reference. (c) FT curves of Fe *K*-edge EXAFS $k^3\chi(k)$ functions of α-Fe_2O_3 nanosheets and bulk α-Fe_2O_3 (inset: $k^3\chi(k)$ curves). (d) Side and top views of the distortion model.

bulk are displayed in Figure 2a,b, respectively. Evidently, the zero field cooling (ZFC) and field cooling (FC) curves of α-Fe_2O_3 nanosheets superimpose in the temperature region of 150−300 K and diverge substantially in the temperature range of 10−150 K (Figure 2a), suggesting a strong ferromagnetic behavior of α-Fe_2O_3 nanosheets. Moreover, the FC magnetization moment increases with decreasing temperature at an exponential-like manner and becomes apparently larger than the ZFC magnetization moments at below 100 K. In particular, the magnetization loops at 100 K present a clear hysteresis for the α-Fe_2O_3 nanosheets with moderate coercive force (300 Oe) and a large saturated magnetic moment of 0.6 μ_B in Figure 2b. It is of interest that the ferromagnetic response can be extended to room temperature (Figures 2b and S6). In contrast to the anti-ferromagnetic nature of bulk α-Fe_2O_3, these results clearly demonstrate the universal ferromagnetic interactions and ferromagnetic ground state in the half-unit-cell α-Fe_2O_3 semiconductor nanosheets. It is worth noting that a small amount of α-Fe_2O_3 nanocrystals might be present in the nanosheet sample in our chemical preparation process. However, the α-Fe_2O_3 nanocrystal is antiferromagnetic, and the presence of other Fe-related magnetic phases could be ruled out (see details in S2 and S3 of Supporting Information). Hence, the half-unit-cell α-Fe_2O_3 nanosheets show an intrinsic and robust ferromagnetism without the effect of other Fe-related phases. The above results indicate strongly that a magnetic transformation from antiferromagnetic to ferromagnetic of α-Fe_2O_3 is successfully realized by a strategy of two-dimension confinement.

In order to explore the electronic states of ferromagnetic α-Fe_2O_3 nanosheets, X-ray photoelectron spectroscopy (XPS) was performed. As shown in Figure 3a, the XPS spectra of the Fe 2p core level for both of the sheet and bulk are characterized by a Fe $2p_{3/2}$ peak at 711.4 eV, accompanied by a shakeup satellite peak at 719.0 eV, and a Fe $2p_{1/2}$ peak at 724.0 eV. Although the main peaks positions are unvaried, their spectral shapes are different: the Fe $2p_{3/2}$ peak of α-Fe_2O_3 nanosheets shifts to the lower energy side and becomes asymmetric, suggesting that the electronic structures of Fe ions are split and a portion of Fe ions occupy the weak ligand field environment.[27] Meanwhile, the absence of the valley at 716 eV implies that the p−d hybridizing of nanosheets is different from that of the bulk.[28] The XPS results clearly indicate that the electronic structure of Fe ions in α-Fe_2O_3 nanosheets is changed, which is

dx.doi.org/10.1021/ja504088n | J. Am. Chem. Soc. 2014, 136, 10393−10398

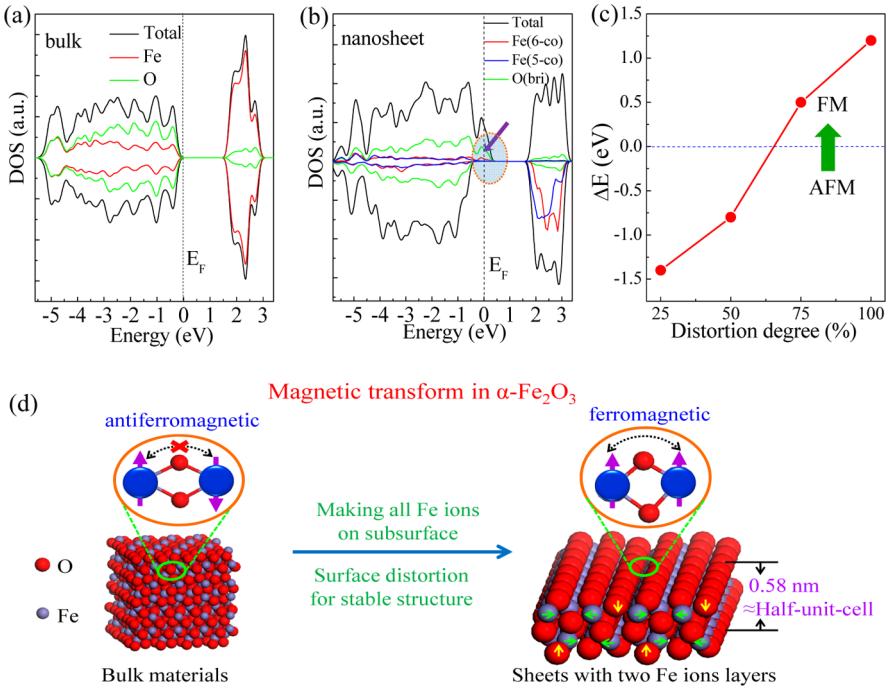

Figure 4. Calculated DOS for bulk (a) and nanosheet (b) α-Fe_2O_3. (c) Function of magnetic exchange energy ($\Delta E = E_{AFM} - E_{FM}$) with the proportion of the $Fe_{5\text{-co}}$-bonded O_{bri} in all O_{bri} atoms. (d) Schematic magnetic interaction turnover model for the α-Fe_2O_3 nanosheets.

likely induced by the distinct Fe−O coordination environments in the nanosheets.

Next, Fe *K*-edge X-ray absorption near-edge structure (XANES) measurements were conducted (Figure 3b). This technique possesses high sensitivity to atomic and electronic structures and helps to determine the local structure around Fe atoms. A clear feature of the pre-edge peak at 7110 eV, corresponding to the Fe 1s → 3d transition, reveals the differences of the Fe coordination environments in the α-Fe_2O_3 nanosheets and bulk counterpart. The pre-edge peak intensity of α-Fe_2O_3 nanosheets is 40% higher than that of bulk α-Fe_2O_3, while it is similar to that of the low-coordinated Fe_3O_4 reference compound,[29,30] suggesting that this spectral characteristic is attributed to the inherent five-coordinated Fe (noted as "$Fe_{5\text{-co}}$" hereafter) of nanosheets. However, the white line peak shape for α-Fe_2O_3 nanosheets is close to that of six-coordinated Fe (noted as "$Fe_{6\text{-co}}$" hereafter) in bulk α-Fe_2O_3. Thus, the XANES results reveal that the nondegenerate $Fe_{5\text{-co}}$ and $Fe_{6\text{-co}}$ coordinations probably coexist in the nanosheets. Furthermore, we calculated the Fe *K*-edge XANES spectra of α-Fe_2O_3 nanosheets using FEFF8.2 code,[31] based on several models with different Fe−O coordination numbers: five-, five-plus six-, and six-coordinated (see details in S3 of Supporting Information). We find that the calculated XANES spectral feature of $Fe_{5\text{-co}}$+$Fe_{6\text{-co}}$ mixed coordination is fairly close to that of the experimental spectrum of α-Fe_2O_3 nanosheets (Figure S11 of Supporting Information). This result provides more evidence that the Fe ions in the synthesized α-Fe_2O_3 nanosheets are in the hybridized states of five- and six-coordinated.

Furthermore, Fe *K*-edge extended X-ray absorption fine structure (EXAFS) measurement was carried out to give quantitative structure information.[32,33] For the Fourier transformed (FT) function of nanosheets in Figure 3c, the peaks at 2.5, 3.3, and 4.7 Å corresponding to the second, third Fe−Fe, and the fourth Fe−O/Fe shells are preserved as those in the bulk, suggesting the retained integrity of hexagonal α-Fe_2O_3 structure in the nanosheets, in agreement with the XRD results. The Fe−O first shell peak is slightly lowered in intensity, and the intensities of the Fe−Fe peaks are significantly reduced by 40%, compared to those of bulk. This indicates that the Fe−Fe second shell is greatly distorted and its structural homogeneity is reduced. The structural parameters of α-Fe_2O_3 nanosheets were obtained and are shown in Table S1 via a least-squares curve parameter fitting based on the model of (110) exposed facet (S3 and Figure S10 of Supporting Information). The obtained coordination number 5.3 for the Fe−O first shell is slightly larger than that of the ideal nanosheets, further confirming the $Fe_{5\text{-co}}$+$Fe_{6\text{-co}}$ mixed coordination deduced from the above XANES analysis. Hence, it can be approximated that about 30% Fe ions take the six-coordinated sites, and about 70% of Fe ions take the five-coordinated sites. Based on the ideal half-unit-cell thickness α-Fe_2O_3 structure, we consider that surface bridge O ions (noted by "O_{bri}" hereafter) may wedge into the nanosheet to bind with another $Fe_{5\text{-co}}$, resulting in the formation of six-coordinated Fe ions. Consequently, the shorter Fe−O bond length is elongated from 1.94 to 1.98 Å, while the longer one is contracted from 2.12 to 2.06 Å (Table S1), enhancing the structural homogeneity of the Fe−O first shell. Also, the Fe−Fe bond lengths are split into one long and one short as shown in Table S1, which is attributed to the shift of Fe ions away from their original positions caused by O_{bri} wedging displacement.

Based on the systematic analyses of the structural parameters of α-Fe_2O_3 nanosheets from XPS, XANES, AFM, HRTEM, and XAFS, a real structure model is established in Figure 3d. In particular, the possibility of surface combination of abundant alien O ions is excluded through the atomic stoichiometry and structural distortion analyses (see details in S5 of Supporting Information). The calculated density of states (DOS) spectra in Figure 4 clearly show that the spin-up 3d states of $Fe_{5\text{-co}}$ ions are all below the Fermi level, with the main peak located at −1

dx.doi.org/10.1021/ja504088n | J. Am. Chem. Soc. 2014, 136, 10393−10398

eV. In contrast, the spin-up 3d states of $Fe_{6\text{-co}}$ ions are much delocalized, pushing the e_g energy states to above the Fermi level by 0.4 eV (Figure 4a,b). The DOS results of the nanosheets suggest that the quantum degeneracy of Fe 3d energy states is successfully broken by the coexistence of five- and six-coordinated Fe ions. The electron exchange between $Fe_{5\text{-co}}$ and $Fe_{6\text{-co}}$ is realized in the nanosheets because the electron transition from the occupied 3d states of $Fe_{5\text{-co}}$ to the empty 3d states of $Fe_{6\text{-co}}$ is permitted according to the Hund's rule.[34,35] This electronic configuration can be further confirmed via temperature-dependent conductivity measurements (Figure S7). The results show 3−5 times enhancement of conductivity in α-Fe_2O_3 nanosheets, and the activation energy of free carriers is lowered by ∼0.3 eV.

As a result, the spin-polarized electrons can transfer along $Fe_{5\text{-co}}$−O_{bri}−$Fe_{6\text{-co}}$ chains freely by hopping between the nondegenerate quantum 3d energy states of $Fe_{5\text{-co}}$ and $Fe_{6\text{-co}}$ ions, greatly reducing the energy of the system via the double exchange effect (Figure 4d and Figure S15). Hence, the spin-exchange interaction between $Fe_{5\text{-co}}$ and neighboring $Fe_{6\text{-co}}$ ions is tuned to ferromagnetic from antiferromagnetic with a large exchange energy ($E_{ex} = E_{AFM} - E_{FM}$) of 1220 meV. The equivalent magnetic moment is 0.8−1.3 μ_B/atom, in good agreement with the experimental magnetic measurements. Further calculations exhibit that the exchange energy E_{ex} can be changed from negative to positive as the $Fe_{6\text{-co}}$ proportion is above 10%, confirming that this ferromagnetic interaction is effective within a wide range of $Fe_{6\text{-co}}$ proportions (Figure 4c). Recently, the synthetic nanosheets of three-layer thick Co_9Se_8 and six-layer thick VSe_2 also presented weak ferromagnetism of <0.01 μ_B/atom saturation moment in contrast with the antiferromagnetic bulk ones.[17] Considering the conductivity measurement results, the observed ferromagnetism in α-Fe_2O_3 nanosheets might be attributed to the permitted electron exchange between the TM ions with the asymmetric 3d energy states.

Figure 4b exhibits that the occupied spin-up and spin-down 3d states of Fe ions are asymmetric and only the spin-up 3d states extend above the Fermi level, revealing a large spin-polarization of the α-Fe_2O_3 nanosheets. This promises a broad prospect for α-Fe_2O_3 nanosheets applied in the future visible-light manipulation spintronic nanodevices and magneto-resistance-based information storage devices. From the above discussions, the key of the magnetic transformation in α-Fe_2O_3 nanosheets lies in the successful realization of structural distortion and coordination environment splitting around the transition-metal ions (as depicted in Figure 4d). This mechanism is similar to that of half-metal magnet Fe_3O_4, in which the ferromagnetism arises from the exchange interactions of Fe ions with different valence states.[36−39] Similar to the bulk α-Fe_2O_3, numerous TMO semiconductors such as NiO, CoO, and MnO_2 exhibit antiferromagnetic characters.[40−42] This means that abundant ferromagnetic semiconductors could be created through the strategy presented in this work. In particular, it could be expected that the geometric morphology of this kind of freestanding nanosheet magnetic semiconductors provides us an excellent platform to tune the magnetic behaviors (Curie temperature, coercivity, and saturation magnetization), through surface functionalizing, charge doping, and thickness control. This work thus demonstrates a novel technical route to prepare practical electron spin-injection source for the development of function-maximized but shape-minimized transparent and flexible spintronics devices.

CONCLUSIONS

In summary, by means of a template-assisted oriented growth strategy, we have realized atomically thin α-Fe_2O_3 nanosheets with half-unit-cell thickness for the first time. The half-unit-cell α-Fe_2O_3 semiconductor nanosheet samples exhibit the intrinsic and robust ferromagnetism of 0.6 μ_B saturation magnetic moment at 100 K and retained a ferromagnetic response at room temperature, comparable with that of traditional half-metal magnets. Since the α-Fe_2O_3 nanocrystal is antiferromagnetic, the observed large magnetic moment can be attributed to the antiferromagnetism to ferromagnetism transformation in 2D α-Fe_2O_3 nanosheets. Structural analyses revealed that the surface distortion of the 2D nanosheets makes a significant proportion (ca. 30%) of five-coordinated Fe ($Fe_{5\text{-co}}$) ions in ideal nanosheets into Fe ($Fe_{6\text{-co}}$) coordinated by six O atoms. The coexistence of $Fe_{5\text{-co}}$ and $Fe_{6\text{-co}}$ ions breaks the quantum degeneracy of Fe 3d energy states in bulk α-Fe_2O_3 and permits an effective electron exchange to activate the ferromagnetic exchange interaction in the α-Fe_2O_3 nanosheets. These intrinsic ferromagnetic α-Fe_2O_3 nanosheets will not only inspire extensive interests in manipulating ferromagnetism in nano-TMO semiconductor materials via 2D strategy but also provide a new candidate for the next-generation miniature spintronic devices.

EXPERIMENTAL SECTION

Sample Synthesis. A facile and controllable bottom-up template growth method was developed to fabricate the half-unit-cell thick α-Fe_2O_3 nanosheets. Specially, 30 mg of CuO nanoplates, which were synthesized by hydrothermal reaction of mixed solution of CuCl and ammonia in Teflon-lined stainless steel autoclave at 150 °C for 20 h, was dispersed into 70 mL of deionized water by sonication for 20 min, then this solution was bubbled by nitrogen for another 20 min; afterward, 30 mg of $FeCl_2{\cdot}H_2O$ was added into the solution. The mixture was sealed in a beaker and maintained at room temperature (25 °C) for a day, then the transparent pale yellow supernatant was transferred into a Teflon-lined autoclave and maintained at 170 °C for 2 h. Finally, a transparent bright red solution was obtained, and the supernatant was centrifuged and washed using a mixture of ammonia (37%) and deionized water (v/v = 1/1) three times to remove the residual CuO, followed by deionized water and ethanol, and finally dried in vacuum at 60 °C overnight for characterization. The result of inductively coupled plasma (ICP) measurement showed that there was a negligible amount of residual Cu (only ∼0.01 wt %) in the final product.

Characterization. Transmission electron microscopy, high-resolution TEM (HRTEM), selected area electron diffraction patterns, and energy-dispersive spectroscopy were performed by using a JEOL-2010 TEM with an acceleration voltage of 200 kV. The field emission scanning electron microscopy images were taken on a FEI Sirion-200 scanning electron microscope. XRD patterns were recorded by using a Philips X'Pert Pro Super diffractometer with Cu Kα radiation (λ = 1.54178 Å). Atomic force microscopy study in the present work was performed by means of Veeco DI Nanoscope MultiMode V system. X-ray photoelectron spectra were acquired on an ESCALAB MKII with Mg Kα ($h\nu$ = 1253.6 eV) as the excitation source. The binding energies obtained in the XPS spectral analysis were corrected for specimen charging by referencing C 1s to 284.5 eV. The ICP mass spectrometry was carried out at plasma atomic emission spectrometry (Atomscan Advantage). The magnetization was characterized by a superconducting quantum interference device (SQUID, quantum design MPMS XL-7) magnetometer with a temperature range of 10−300 K and applied field range of −20000 to 20000 Oe. The electrical conductivity was measured on a Keithley 4200 station with the computer-controlled four-probe technique. To accurately measure the conductivity, the samples were pressed into a pellet and then were cut

dx.doi.org/10.1021/ja504088n | J. Am. Chem. Soc. 2014, 136, 10393−10398

into rectangular shape with a size of 10 mm × 10 mm × 1 mm; after that, they were attached to four copper wires on the surface with silver paste to improve contact performance. The X-ray absorption find structure data were collected at U7C station in NSRL, BL14W1 station in SSRF, and 1W1B station in BSRF. The storage rings of NSRL, SSRF, and BSRF were operated at 0.8 GeV with the current of 250 mA, at 3.5 GeV with the current of 300 mA, and at 2.5 GeV with a maximum current of 250 mA, respectively.

■ ASSOCIATED CONTENT

Supporting Information

Fast Fourier transform image of HRTEM, temperature-dependent conductivity, XPS spectra, XRD pattern and TEM image of bulk α-Fe_2O_3, XAFS measurement and data analysis, and density functional theory calculation details and analysis. This material is available free of charge via the Internet at http://pubs.acs.org.

■ AUTHOR INFORMATION

Corresponding Authors

qhliu@ustc.edu.cn
ywsh2000@ustc.edu.cn
sqwei@ustc.edu.cn

Author Contributions

†W.R.C. and J.F.H. contributed equally to this work.

Notes

The authors declare no competing financial interest.

■ ACKNOWLEDGMENTS

This work was supported by the National Natural Science Foundation of China (Grant Nos. 11135008, 11105151, U1332111, U1332131, and U1232132), the National Basic Research Program of China (2012CB825800), and the Foundation for Innovative Research Groups of the National Natural Science Foundation of China (11321503). The authors would like to thank NSRL, SSRF, and BSRF for the synchrotron beamtime.

■ REFERENCES

(1) Geim, A. K. *Science* **2009**, *324*, 1530−1534.
(2) Zhang, X. D.; Xie, Y. *Chem. Soc. Rev.* **2013**, *42*, 8187−8199.
(3) Wang, Y.; Wang, X. C.; Antonietti, M. *Angew. Chem., Int. Ed.* **2012**, *51*, 68−89.
(4) Schwierz, F. *Nat. Nanotechnol.* **2010**, *5*, 487−496.
(5) Wang, Q. H.; Kalantar-Zadeh, K.; Kis, A.; Coleman, J. N.; Strano, M. S. *Nat. Nanotechnol.* **2012**, *7*, 699−712.
(6) Chhowalla, M.; Shin, H. S.; Eda, G.; Li, L. J.; Loh, K. P.; Zhang, H. *Nat. Chem.* **2013**, *5*, 263−275.
(7) Sun, Y. F.; Cheng, H.; Gao, S.; Sun, Z. H.; Liu, Q. H.; Liu, Q.; Lei, F. C.; Yao, T.; He, J. F.; Wei, S. Q.; Xie, Y. *Angew. Chem., Int. Ed.* **2012**, *51*, 8727−8731.
(8) Nicolosi, V.; Chhowalla, M.; Kanatzidis, M. G.; Strano, M. S.; Coleman, J. N. *Science* **2013**, *340*, 1420.
(9) Coleman, J. N.; Lotya, M.; O'Neill, A.; Bergin, S. D.; King, P. J.; Khan, U.; Young, K.; Gaucher, A.; De, S.; Smith, R. J.; Shvets, I. V.; Arora, S. K.; Stanton, G.; Kim, H. Y.; Lee, K.; Kim, G. T.; Duesberg, G. S.; Hallam, T.; Boland, J. J.; Wang, J. J.; Donegan, J. F.; Grunlan, J. C.; Moriarty, G.; Shmeliov, A.; Nicholls, R. J.; Perkins, J. M.; Grieveson, E. M.; Theuwissen, K.; McComb, D. W.; Nellist, P. D.; Nicolosi, V. *Science* **2011**, *331*, 568−571.
(10) Ciesielski, A.; Samori, P. *Chem. Soc. Rev.* **2014**, *43*, 381−398.
(11) Xu, M. S.; Liang, T.; Shi, M. M.; Chen, H. Z. *Chem. Rev.* **2013**, *113*, 3766−3798.
(12) Busch, M.; Ahlberg, E.; Panas, I. *Catal. Today* **2013**, *202*, 114−119.
(13) Chakrabarty, S.; De, K.; Das, S.; Amaral, V. S.; Chatterjee, K. *J. Nanosci. Nanotechnol.* **2014**, *14*, 4236−4244.
(14) Zhu, J. B.; Bai, L. F.; Sun, Y. F.; Zhang, X. D.; Li, Q. Y.; Cao, B. X.; Yan, W. S.; Xie, Y. *Nanoscale* **2013**, *5*, 5241−5246.
(15) Yao, T.; Liu, L.; Xiao, C.; Zhang, X. D.; Liu, Q. H.; Wei, S. Q.; Xie, Y. *Angew. Chem., Int. Ed.* **2013**, *52*, 7554−7558.
(16) Schliehe, C.; Juarez, B. H.; Pelletier, M.; Jander, S.; Greshnykh, D.; Nagel, M.; Meyer, A.; Foerster, S.; Kornowski, A.; Klinke, C.; Weller, H. *Science* **2010**, *329*, 550−553.
(17) Zhang, X. D.; Zhang, J. J.; Zhao, J. Y.; Pan, B. C.; Kong, M. G.; Chen, J.; Xie, Y. *J. Am. Chem. Soc.* **2012**, *134*, 11908−11911.
(18) Liu, X. H.; Ma, R. Z.; Bando, Y.; Sasaki, T. *Adv. Mater.* **2012**, *24*, 2148−2153.
(19) Compton, O. C.; Abouimrane, A.; An, Z.; Palmeri, M. J.; Brinson, L. C.; Amine, K.; Nguyen, S. T. *Small* **2012**, *8*, 1110−1116.
(20) Chou, S. S.; De, M.; Kim, J.; Byun, S.; Dykstra, C.; Yu, J.; Huang, J. X.; Dravid, V. P. *J. Am. Chem. Soc.* **2013**, *135*, 4584−4587.
(21) Kai, K.; Yoshida, Y.; Kageyama, H.; Saito, G.; Ishigaki, T.; Furukawa, Y.; Kawamata, J. *J. Am. Chem. Soc.* **2008**, *130*, 15938−15943.
(22) Wang, L. L.; Fei, T.; Lou, Z.; Zhang, T. *ACS Appl. Mater. Interfaces* **2011**, *3*, 4689−4694.
(23) Chen, L. Q.; Yang, X. F.; Chen, J. A.; Liu, J.; Wu, H.; Zhan, H. Q.; Liang, C. L.; Wu, M. M. *Inorg. Chem.* **2010**, *49*, 8411−8420.
(24) Jung, Y.; Son, Y. H.; Lee, J. K. *RSC Adv.* **2012**, *2*, 5877−5884.
(25) Zhu, J. X.; Yin, Z. Y.; Yang, D.; Sun, T.; Yu, H.; Hoster, H. E.; Hng, H. H.; Zhang, H.; Yan, Q. Y. *Energy Environ. Sci.* **2013**, *6*, 987−993.
(26) Huang, L. Z.; Hassenkam, T.; Hansen, H. C. B.; Bjerrum, M. J. *J. Mater. Chem. A* **2014**, *2*, 4029−4037.
(27) Castro, L.; Dedryvere, R.; El Khalifi, M.; Lippens, P. E.; Breger, J.; Tessier, C.; Gonbeau, D. *J. Phys. Chem. C* **2010**, *114*, 17995−18000.
(28) Fujii, T.; de Groot, F. M. F.; Sawatzky, G. A.; Voogt, F. C.; Hibma, T.; Okada, K. *Phys. Rev. B* **1999**, *59*, 3195−3202.
(29) Westre, T. E.; Kennepohl, P.; DeWitt, J. G.; Hedman, B.; Hodgson, K. O.; Solomon, E. I. *J. Am. Chem. Soc.* **1997**, *119*, 6297−6314.
(30) Wilke, M.; Farges, F.; Petit, P. E.; Brown, G. E.; Martin, F. *Am. Mineral.* **2001**, *86*, 714−730.
(31) Ankudinov, A. L.; Ravel, B.; Rehr, J. J.; Conradson, S. D. *Phys. Rev. B* **1998**, *58*, 7565−7576.
(32) Yao, T.; Sun, Z. H.; Li, Y. Y.; Pan, Z. Y.; Wei, H.; Xie, Y.; Nomura, M.; Niwa, Y.; Yan, W. S.; Wu, Z. Y.; Jiang, Y.; Liu, Q. H.; Wei, S. Q. *J. Am. Chem. Soc.* **2010**, *132*, 7696−7701.
(33) Yao, T.; Zhang, X. D.; Sun, Z. H.; Liu, S. J.; Huang, Y. Y.; Xie, Y.; Wu, C. Z.; Yuan, X.; Zhang, W. Q.; Wu, Z. Y.; Pan, G. Q.; Hu, F. C.; Wu, L. H.; Liu, Q. H.; Wei, S. Q. *Phys. Rev. Lett.* **2010**, *105*, 226405.
(34) Gutzwiller, M. C. *Phys. Rev. Lett.* **1963**, *10*, 159.
(35) Hubbard, J. *Proc. R. Soc. London* **1963**, *276*, 238.
(36) Sun, S. H.; Zeng, H. *J. Am. Chem. Soc.* **2002**, *124*, 8204−8205.
(37) Dutta, P.; Manivannan, A.; Seehra, M.; Shah, N.; Huffman, G. *Phys. Rev. B* **2004**, *70*, 174428.
(38) Singh, M.; Ulbrich, P.; Prokopec, V.; Svoboda, P.; Šantavá, E.; Štěpánek, F. *J. Magn. Magn. Mater.* **2013**, *339*, 106−113.
(39) Sun, S. H.; Zeng, H.; Roubinson, D. B.; Raoux, S.; Rice, P. M.; Wang, S. X.; Li, G. X. *J. Am. Chem. Soc.* **2003**, *126*, 273−279.
(40) Michele, C.; Giovanni, S. *Faraday Discuss.* **1997**, *106*, 189−203.
(41) Rödl, C.; Bechstedt, F. *Phys. Rev. B* **2012**, *86*, 235122.
(42) Choukroun, J. *Phys. Rev. B* **2011**, *84*, 014415.